Rare Met. (2018) 37(11):919–928
https://doi.org/10.1007/s12598-018-1064-4

RARE METALS
www.editorialmanager.com/rmet

Enhance of TiO_2 dopants incorporated reduced graphene oxide via RF magnetron sputtering for efficient dye-sensitised solar cells

Foo Wah Low, Chin Wei Lai*, Kian Mun Lee, Joon Ching Juan

Received: 26 January 2018 / Revised: 22 March 2018 / Accepted: 21 April 2018 / Published online: 30 May 2018

Abstract In particular, the dye-sensitised solar cells (DSSCs) have a high potential in the rational energy conversion efficiency to secure our sustainable energy source. In the present study, advanced radio frequency (RF) magnetron sputtering technique was applied to incorporate titanium dioxide (TiO_2) dopants into reduced graphene oxide (rGO) nanosheet for improving the power conversion efficiency (PCE) of DSSCs device. An optimum TiO_2 content incorporated onto rGO nanosheet plays an important role in improving the PCE of DSSCs by minimising the recombination losses of photo-induced charge carriers. Based on the results obtained, 40-s sputtering duration for incorporating TiO_2 dopants onto rGO nanosheet exhibits a maximum PCE of 8.78% than that of pure rGO film (0.68%). In fact, the presence of optimum content of TiO_2 dopants within rGO nanosheet could act as mediators for efficient separation photo-induced charge carriers. However, the excessive of sputtering duration (e.g. 60 s) of TiO_2 dopants onto rGO nanosheet results higher charge recombination and lowers the PCE of DSSCs (5.39%).

Keywords Dye-sensitised solar cell; RF magnetron sputtering; Titanium dioxide; Reduced graphene oxide

1 Introduction

In the last decade, different approaches of synthesis have been adopted to obtain an active TiO_2–rGO nanocomposite photocatalyst with high efficiency [1–3]. It is believed that the physico-chemical characteristics of the rGO nanosheet thin film could be improved via the incorporation of the TiO_2 dopants for dye-sensitised solar cells (DSSCs) device [1–5]. To date, some conventional synthesis techniques, namely molecular grafting, spray drying and dispersion, have been conducted to form TiO_2–rGO nanocomposite film to enhance the PCE of DSSCs device. According to the literature surveys, one-step hydrothermal synthesis appears as the most prominent process that applies single or heterogenous phase reaction to crystallise TiO_2–rGO nanocomposite directly from solution at an elevated temperature and pressure. In this way, the lattice defect matter of the TiO_2–rGO nanocomposite was greatly reduced [6–9]. However, the main drawbacks of this technique are the use of costly autoclaves system, a considerable size of good quality seeds and the difficulties in controlling the crystal growth for TiO_2–rGO nanocomposite [8, 10]. Table 1 summarised some recent works on different approaches for the formation of TiO_2–rGO nanocomposite in DSSCs application [4, 10–27].

It has been reported that the coupling between TiO_2 and rGO via deposition could enhance the charge carrier separation efficiency and good visible light response for DSSCs device [11–13]. It was observed that the TiO_2–rGO nanocomposite photoanode showed a higher PCE and photocurrent density (J_{sc}) in the DSSCs device as compared to the TiO_2 photoanode alone [14, 15]. In fact, all recent works have reported that TiO_2–rGO nanocomposite photoanode has gained much attention due to the unique features of high photocatalysis activity, great absorptivity of dyes, extended light absorption to visible range and rapid electron mobility to suppress the charge carrier recombination [16]. Moreover, the band gap of the TiO_2–

F. W. Low, C. W. Lai*, K. M. Lee, J. C. Juan
Nanotechnology and Catalysis Research Centre, Institute Postgraduate Studies, University of Malaya, 50603 Kuala Lumpur, Malaysia
e-mail: cwlai@um.edu.my

Table 1 Summary of recent works reported on different approaches in formation of TiO_2–rGO nanocomposite in DSSCs application

Photoanode materials	Synthesis method	Reference cell	Optimised content of rGO	Reference cell of photoanode				Improved of TiO_2–rGO photoanode			
				J_{sc}/(mA·cm^{-2})	V_{oc}/V	*ff*	η/%	J_{sc}/(mA·cm^{-2})	V_{oc}/V	*ff*	η/%
TiO_2 with rGO (from GO) [4]	Molecular grafting	$Ti(OBu)_4$	With/without rGO incorporation	1.95	0.52	0.31	0.32	6.67	0.56	0.45	1.68
P25-Rgo [10]	–	P25	0.050 wt%	5.04	n/a	n/a	2.70	8.38	n/a	n/a	4.28
TiO_2 with rGO (from GO) [11]	Spray drying	TiO_2	Device comparison	16.40	0.60	0.52	5.09	18.20	0.58	0.58	6.06
P25-rGO [12]	n/a	P25	1.00 wt%	18.83	0.69	0.46	5.98	19.92	0.70	0.49	6.86
TiO_2 with rGO (from GO) [13]	Solvothermal	P25	Ultra-small 2 nm TiO_2–rGO nanosheets	6.20	0.67	0.69	2.85	13.50	0.77	0.70	7.25
TiO_2 with rGO (from GO) [14]	Dispersion	TiO_2 nanosheets	0.750 wt%	13.70	0.59	0.57	4.61	16.80	0.61	0.57	5.77
TiO_2–rGO [15]	Hydrothermal	P25	1.000 wt%	11.90	0.68	0.61	4.96	18.30	0.74	0.56	7.54
CdS- TiO_2–rGO [16]	Hydrothermal	$Ti(OBu)_4$	8 mg	4.74	0.55	0.42	1.08	7.19	0.58	0.41	1.70
TiO_2–rGO [17]	Grätzel	P25	0.750 wt%	10.75	0.69	0.57	4.20	12.16	0.67	0.68	5.50
P25-rGO [18]	Dispersion	P25	1.000 wt%	11.90	0.69	0.61	4.96	15.40	0.67	0.64	6.58
TiO_2–rGO [19]	CVD	TiO_2	Multilayer oxygenated rGO–TiO_2	12.70	0.70	n/a	5.60	16.0	0.73	n/a	6.70
TiO_2–rGO inverse opal [20]	Infiltrated	TiO_2 inverse opal	3.000 wt%	12.39	0.66	0.60	4.86	17.10	0.72	0.61	7.52
TiO_2–rGO [21]	Hydrothermal	$Ti(OBu)_4$	n/a	7.85	0.66	0.60	3.11	10.07	0.75	0.57	4.28
TiO_2–rGO [22]	n/a	TiO_2	0.005 wt%	12.22	0.65	n/a	3.50	13.55	0.68	n/a	4.03
TiO_2–rGO [23]	Hydrothermal	450 °C TiO_2–rGO	550 °C	13.65	0.69	0.51	4.85	14.17	0.74	0.51	5.34
Ti with rGO (from GO) [24]	Hydrothermal	TTIP	Method comparison	15.26	0.68	0.59	5.82	18.46	0.73	0.69	8.62
Ti-rGO [25]	Sonication	TiO_2	0.010 wt%	6.27	0.71	0.60	2.68	8.42	0.68	0.64	3.69
TiO_2–rGO [26]	Hydrothermal	TiO_2	0.500 mg·ml^{-1}	6.93	0.62	0.65	2.82	12.13	0.65	0.64	5.08
rGO (from GO) with TiO_2 [27]	Thermal reduction	TiO_2	n/a	10.14	0.68	0.67	4.60	11.06	0.67	0.74	5.50

J_{sc} short-circuit current density, V_{oc} open-circuit voltage, *ff* fill factor and η power conversion efficiency

rGO nanocomposite was reduced significantly [17, 18]. The main reason is due to the formation of Ti–O-C bond and the hybridisation of C $2p^2$ orbitals and O $2p^4$ orbitals to form a new valence band.

The synthesis of a high-quality TiO_2–rGO nanocomposite is inevitable to be applied as an efficient photoanode in DSSCs device [19]. In present study, the high-quality TiO_2–rGO junction of photoanode with uniform homogeneity was decorated by radio frequency (RF) magnetron sputtering technique [20]. This technique is better than that of conventional synthesis methods due to the easy incorporation of the high-energy Ti^{4+} species in a much shorter time [20–22]. However, the high kinetic bombardment of Ti^{4+} species towards rGO nanosheets will easily cause some structural damage and defects. Indeed, RF magnetron sputtering technique is widely used to construct a uniform, well crystallised and large-area composite film. This is due to the fact that the characteristics of the film can be easily controlled by adjusting the sputtering power, substrate temperature, partial pressure of sputtering, sputtering duration and distance from target to the substrate.

Theoretically, the RF magnetron sputtering technique allows for a much better adhesion of TiO_2 dopants on rGO nanosheets due to the deposited Ti^{4+} species which possess a higher kinetic energy [20]. Therefore, these species can be effectively implanted deeply into rGO lattice through atomic layers. Moreover, the positively charged Ti^{4+} species generated in the plasma region are easily attracted to

the rGO nanosheets. To date, reports regarding the formation of TiO_2–rGO nanocomposite film through RF magnetron sputtering technique that resulted in enhanced the photoelectrochemical cell of DSSCs are still lacking. The relationship between the sputtering duration towards the thin rGO nanosheets and their DSSCs performance remains unclear [23]. Thus, comprehensive studies were conducted to optimise the sputtering duration in order to obtain the desired TiO_2–rGO nanocomposite film, which exhibits a promising DSSCs performance under solar illumination.

2 Experimental

2.1 Preparation of rGO nanosheets

In the present study, GO was synthesised from the graphite flakes (Sigma-Aldrich) using a facile Improved Hummer's method, while the rGO was obtained by applying the chemical reduction method [24]. In a typical synthesis, an approximately 9 g $KMnO_4$ was added into a mixture solution containing 1.5 g graphite flakes powders and H_2SO_4:H_3PO_4 (9:1). The overall process was reacted in an ice–water bath condition (< 20 °C) while the mixture was stirred for 24 h. Then, the mixture was cooled to room temperature and poured slowly to 200 ml deionized (DI) water and 1 µl hydrazine was added instantly. Then, the mixture solution was immersed into an oil bath (80 °C) before being centrifuged to remove excess impurities.

2.2 Preparation of TiO_2–rGO photoanode

In the formation of hybrid TiO_2–rGO photoanode, the rGO nanosheets were coated onto the FTO (fluorine doped tin oxide) glass slide (20 mm × 20 mm) via an electrodeposition method. Then, a RF magnetron sputtering process was carried out to deposit high accelerated Ti^{4+} onto the rGO nanosheets using RF sputtering machine (Penta Vacuum) with titanium target (99.99% purity, diameter in 50,800 µm and thickness in 6350 µm). The target distance was fixed at 10 cm between Ti targets and the sample while Ar gas flow rate at 15 ml·min^{-1}. In order to avoid surface contaminants, there was a pre-sputtering flow by pure Ar gas for 15 min. Besides, the base pressure is 0.67 mPa and sputter process pressure at constant 266.64 mPa. The duration of sputtering was varied (10, 20, 30, 40 and 60 s) at a constant power discharge of 150 W. The resultant samples were identified as TG10s, TG20s, TG30s, TG40s and TG60s, respectively. In the next stage, a custom-designed DSSCs device consisting of TiO_2–rGO photoanode, cathode, N-719 dye and KI electrolyte was fabricated for PCE performance evaluation.

2.3 Characterisations

The phase determination of the synthesised hybrid TiO_2–rGO nanocomposites was characterised by a X-ray diffractometer (XRD, D8 Advance Bruker AXS) with Cu Kα radiation (λ = 0.15418 nm), operated at 40 kV and 30 mA. The surface morphologies of the hybrid TiO_2–rGO nanocomposites were viewed by field emission scanning electron microscope (FESEM, FEI Quanta 200 FEG), and high-resolution transmission electron microscopy (HRTEM, JEM 2100-F) operated at 200 kV. The elemental analysis of the hybrid nanocomposites samples was determined using energy-dispersion X-ray (EDX) equipped with FESEM. Next, photoluminescence (PL) and Raman spectra were obtained at room temperature using a Renishaw in Via microscope (HeCd laser source, λ = 514.0 nm). The optical properties of hybrid nanocomposites samples were further determined via a UV–visible-diffuse reflectance spectrophotometer (UV-2600, Shimadzu Co.). Photoelectron spectra were obtained through X-ray photoelectron spectroscopy (XPS, PHI Quantera II instrument) with a dual X-ray source. All binding energies were calibrated using contaminant carbon (C 1s, 284.6 eV) as a reference. A 150 W xenon lamp (Newport 66,902 instrument) was used to produce a largely continuous and uniform spectrum. The DSSCs device was connected to a potentiostat (PGSTAT204), and the current and voltage were measured.

3 Results and discussion

XRD patterns of pure of rGO, anatase TiO_2 and TiO_2–rGO nanocomposite which were subjected to different sputtering time are presented in Fig. 1. It could be observed that all TiO_2–rGO nanocomposite samples hinder the

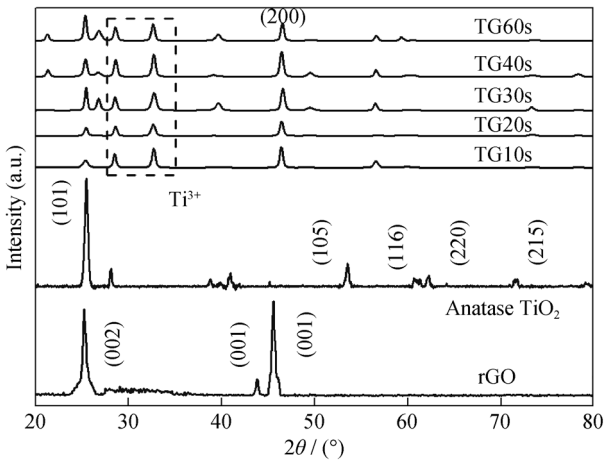

Fig. 1 XRD patterns of rGO, anatase TiO_2 and TiO_2–rGO nanocomposite sputtered for 10, 20, 30, 40 and 60 s

crystallisation of TiO_2 significantly [16]. The intensity of the (101) peak at 25.3° increases by increasing the sputtering time, indicating that the crystallinity of the anatase phase of TiO_2 on rGO nanosheet increases significantly. The appearance of two obvious peaks at 28.2° and 32.3° in XRD patterns proves that the presence of Ti^{3+} species are loaded onto rGO nanosheet. Indeed, the resultant Ti^{3+} species are released from Ti^{4+} [$Ti^{4+} \rightarrow Ti^{3+} + e^-$] through the shift of electrons from the conduction band (CB) of rGO (− 4.4 eV) to the lower-lying CB of TiO_2 (− 4.2 eV). In this manner, small Ti^{4+} species from titanium target might be located at the interstitial sites of rGO lattice and eventually form Ti–O–C bonds to perform high electrons transportation rate.

In present study, UV–Vis-diffuse reflectance spectra (UV-DRS) spectroscopy was applied to study the optical properties of synthesised TiO_2–rGO nanocomposite. The reflectance spectra can then be transformed into Tauc plot (Fig. 2b) by applying the Kubelka–Munk (K–M) expression shown in Eq. (2).

$$F(R) = (1 - R)^2/2R \quad (1)$$

$$F(R) * hv = A\left(hv - E_g\right)^2 \quad (2)$$

where E_g is band gap energy; $F(R)$ is K–M function; R is reflectance; h is Plank's constant; v is the ratio of speed of light to wavelength; and A is constant.

Figure 2a, b shows the absorbance and Tauc plot of TiO_2–rGO nanocomposite sputtered for 10, 20, 30, 40 and 60 s, respectively. Interestingly, the TG40s sample is remarkably substantially red and shifted to the higher wavelength in the absorption edge as compared to the TG60s. A red shift of the peak for TG40s sample infers that the band gap narrowing after rGO nanosheet is sputtered for different time up to 60 s. Indeed, the reduction in band gap energy for TiO_2–rGO nanocomposite indicates a decrease in charge carrier recombination compared with that of pure rGO and pure TiO_2. The optical band gaps of TiO_2–rGO nanocomposites are determined using Tauc plot of the Kubelka–Munk (KM) function in Fig. 2b. The estimated band gap energies for samples denoted as TG10s–TG60s are approximately 2.89, 2.82, 2.80, 2.60 and 2.90 eV, respectively. Based on the results obtained, the TG40s sample shows the smallest band gap energy of about 2.60 eV. The main reason might be ascribed to the more Ti–O–C bonds which are formed between Ti^{4+} and rGO nanosheet during implantation process. Indeed, the mixing of rGO and TiO_2 which represent p state and O 2*p* orbital in valence band, respectively, in turn shifts the valence band edge of TiO_2 upwards and narrows down the band gap of TiO_2–rGO nanocomposites significantly.

Raman analysis was used to understand the structural changes of rGO nanosheet, anatase TiO_2 and TiO_2–rGO nanocomposite film. In Fig. 3, the obvious Raman modes for rGO are detected at 1350.95 and 1604.96 cm^{-1} which are attributed to the D and G vibration mode, respectively. The D vibration mode represents the defects, edges and disordered carbon (A_{1g} symmetry), whereas G is the first-order scattering of phonons by the sp^2-bonded carbon network (E_{2g} symmetry). Besides, the main broad peak of anatase TiO_2 at 126.26 cm^{-1} is attributed to the main anatase vibration mode, $E_{g(1)}$. Moreover, the presence of crystalline TiO_2 is confirmed by the vibration peaks at 207.27 cm^{-1} for E_g, 372.27 cm^{-1} for $B_{1g(1)}$, 493.62 cm^{-1} for A_{1g} and 611.65 cm^{-1} for $E_{g(2)}$ [25]. The presence of vibration peaks of anatase TiO_2 in TiO_2 decorates the rGO nanosheet (126.26 cm^{-1}) and agrees with the strong interaction between TiO_2 and rGO nanosheet samples. In addition, the decreasing intensity at 126.26 cm^{-1} of TG60s compared with that of TG40s indicates that excess Ti^{4+} are implanted into rGO nanosheet. The disappearance of D (1341.73 cm^{-1}) and G (1596.06 cm^{-1}) vibration peaks in TG10s–TG60s samples is due to the huge intensity peaks of anatase TiO_2 (126.26 cm^{-1}) [25]. It could be noticed that the sample of TG40s which is subjected to 40-s

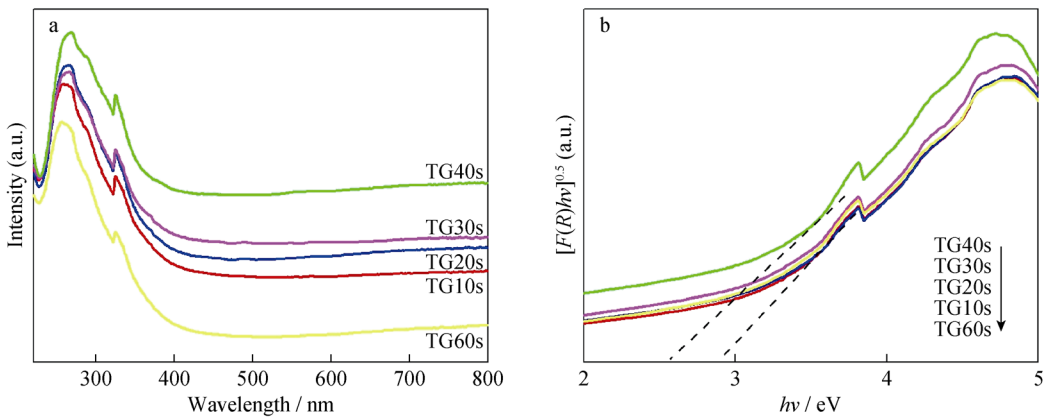

Fig. 2 UV-DRS **a** absorbance spectra and **b** Tauc plot for TiO_2–rGO nanocomposite sputtered at different time

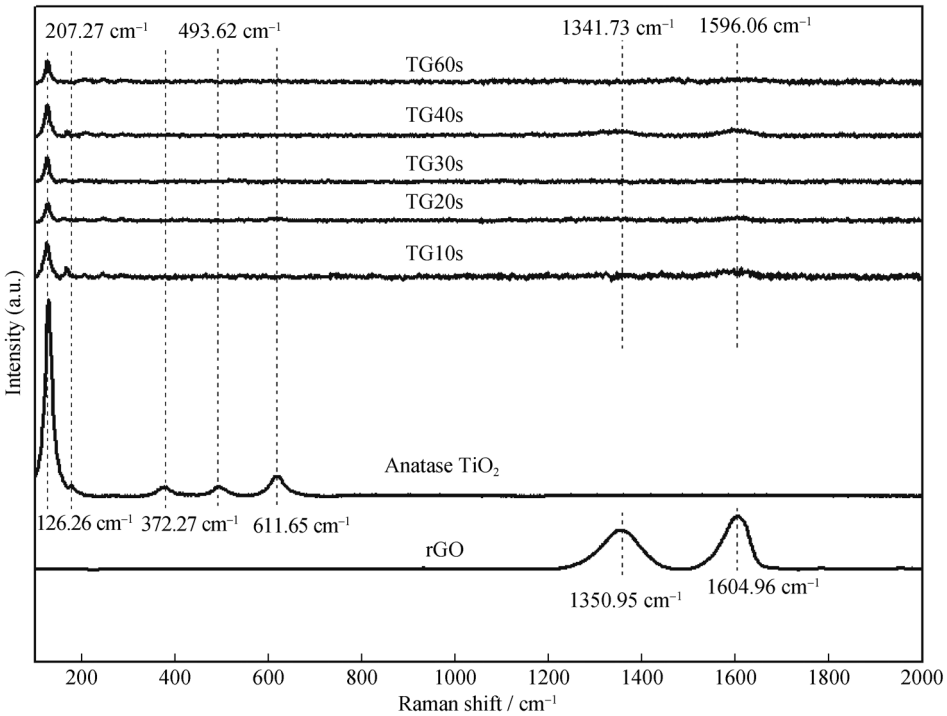

Fig. 3 Raman spectra of rGO, anatase TiO_2 and TiO_2–rGO nanocomposite sputtered for 10, 20, 30, 40 and 60 s

sputtering time shows an insignificant appearance of D and G vibration peaks from Raman modes. In addition, I_D/I_G ratios of TG10s–TG60s are calculated as 0.65, 0.55, 0.34, 0.76 and 0.58 corresponding to TG10s–TG60s samples. I_D/I_G is the ratio of D and G bands of rGO corresponding to the TiO_2–rGO spectra within 1300–1650 cm^{-1}. A maximum I_D/I_G ratio is observed for TG40s sample, which is relatively high compared to those of other samples.

In Fig. 4, the PL spectra of TiO_2–rGO nanocomposites are distributed into three main peaks located at 438, 471 and 494 nm, respectively [26]. Interestingly, the reduction in PL intensity for 40-s sputtered TiO_2–rGO nanocomposite indicates a decrease in the charge carrier

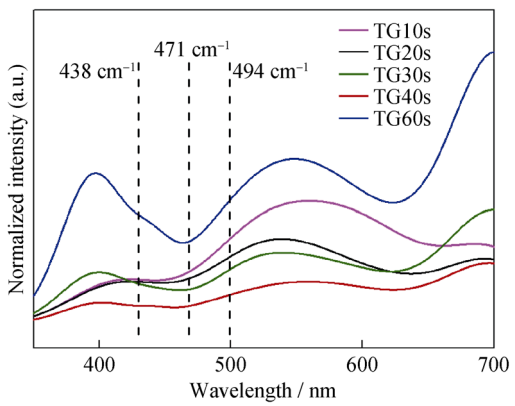

Fig. 4 PL spectra of TiO_2–rGO nanocomposite sputtered for different time

recombination. Since rGO is a good conductor, it assists TiO_2 to overcome electron–holes pair's recombination within the lattice, thus resulting in good photocatalytic activity. The photogenerated electrons from rGO nanosheet transfer to TiO_2 rather than undergo recombination. However, the PL intensity for TiO_2–rGO nanocomposite sputtered for 60 s is found to increase. The observed PL response can be attributed to the high TiO_2 content, which acts as electron/hole pairs recombination centres rather than facilitates the charge transport and reduces the electrolyte redox reaction [27].

The study of the functional groups was further analysed by attenuated total reflection Fourier-transform infrared spectroscopy (ATR-FTIR). The ATR-FTIR was performed by FTIR-Spectrum 400 instrument, Perkin Elmer. For FTIR measurement, the entire scan was from 500 to 4000 cm^{-1}. Figure 5 shows FTIR spectra of rGO and TiO_2–rGO nanocomposite sputtered for 10, 20, 30, 40 and 60 s. In the spectrum of rGO, the peaks at 3425 and 1520 cm^{-1} are assigned to the stretching vibration of hydroxyl groups (–OH) and the skeletal vibration groups (C=C). The other peaks at 1720, 1400, 1220 and 1030 cm^{-1} are ascribed to the vibrations of oxygenated groups carboxyl C=O, carboxyl C–O, epoxide C–O–C or phenolic C–O–H and alkoxy C–O, respectively. FTIR spectra show that most of the oxygenated contained functional groups within the samples (TG10s–TG60s) are eliminated due to the new formation bonding of Ti–O–C or

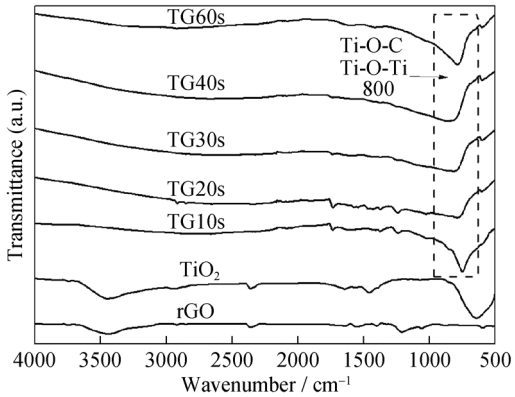

Fig. 5 FTIR spectra of rGO NS and TiO_2–rGO nanocomposite sputtered for different time

Ti–O–Ti within 800–900 cm^{-1} absorption peak. TG60s sample mostly forms Ti–O–Ti rather than Ti–O–C due to the excess of TiO_2 dopants loaded on rGO nanosheet. This phenomenon is attributed to the oxygen containing at 1220 cm^{-1}. An absorption peak of 3425 cm^{-1} decreases dramatically by increasing the sputtering time from 10 to 60 s. TG40s sample shows the most significance in disappearance of oxygen-containing absorption peak (1030, 1220, 1400, 1720 and 3425 cm^{-1}) throughout the potential window. The significant reduction in oxygen-containing absorption peak is mainly accredited to the optimum content of TiO_2 species substituted within the rGO nanosheet, which has an important function in the charge carrier separation.

Subsequently, corresponding FESEM and HRTEM images of the selected TiO_2–rGO nanocomposite sputtered for 40 s are presented in Fig. 6. Figure 6a shows the morphology of rGO nanosheet in multilayers or binary layer system. As the sputtering duration increases to 40 s, a rough and corrugated surface with attachment of small nanoparticles is formed on the surfaces of TR40s (Fig. 6b). EDX results of TR40s sample show that the presence of C, Ti and O are recorded as 20.88 at%, 28.14 at% and 46.24 at%, respectively. Besides, the desertion compounds with 4.74 at% F, Mg and Si are insignificant within TR40s. In these detected irrelevant compound, F compound is obtained from the FTO glass, while Mg compound might be obtained from RF sputtering instrument. Si compound might be contaminated from the conductive tape. Furthermore, the average particle size of TiO_2 is about 61 nm, as shown in Fig. 6c. Next, the lattice of TG40s sample was identified using HRTEM under 2-nm magnification, as presented in Fig. 6d. The darker colour (grey) represents anatase TiO_2 agreement with (101) orientation while lattice is measured as $\sim$ 0.35 nm corresponding with 10 lines whereas brighter colour (white) ascribed to $\sim$ 0.34 nm/10 lines is assigned as graphitic sp^2 carbon network of rGO [1, 28]. Besides, the mixed colour (white and grey) is denoted as TiO_2–rGO where TiO_2 are incorporated with rGO and Ti–O–C bonding is formed.

XPS survey spectra analysis was studied to investigate the chemical state C, Ti and O elements in rGO and representative samples of TiO_2–rGO nanocomposite subjected for 40 s (Fig. 7). The rGO spectrum consists of C 1s and O 1s at 283 and 531 eV, respectively. Furthermore, TG40s shows four main peaks which are C 1s, Ti 2p, O 1s and Ti 2s located at 283, 458, 529 and 564 eV, respectively. The presence of Ti 2p and Ti 2s attributed to the TiO_2 dopants are successfully implanted into rGO nanosheet. Besides, the decrease in C 1s intensity from XPS survey spectra clearly proves that most of the carbon network of rGO structure is broken by high accelerated energy of Ti^{4+} and Ti–O–C bonding is formed. In addition, the O 1s intensity of TG40s sample increases significantly compared with that of rGO nanosheet due to the more oxygen molecules contributed by TiO_2 dopants.

Figure 8 displays C 1*s* XPS spectra of rGO nanosheet and TiO_2–rGO nanocomposite sputtered with 40 s. For rGO (Fig. 8a), one typical peak of C–C located at $\sim$ 284.7 eV is attributed to the graphitic sp^2 carbon atoms and the other three peaks at $\sim$ 285.9, $\sim$ 287.2 and $\sim$ 288.5 eV are assigned to the carbon atoms bonding with oxygenated functional groups such as C–O (epoxy and hydroxyl), C=O (carboxylate) and COOH, respectively [29]. These oxygenated functional groups of rGO nanosheet could act as active sites for directly bonding with TiO_2 dopants to form TiO_2–rGO nanocomposite [30]. The C 1*s* XPS spectra of TG40s sample shows binding energies of 284.5, 285.7 and 288.6 eV. The C 1s broad peak located at $\sim$ 284.5 eV is assigned to graphitic sp^2 carbon atoms peak whereas $\sim$ 285.7 eV is attributed to the defect-containing sp^2 hybridised carbons [31]. Moreover, the weak peak located at $\sim$ 288.6 eV is assigned to the carboxyl carbon functional group (O–C=O), revealing that O=C–O–Ti bonds are formed. The –OH groups from COOH are eliminated during Ti ion implantation process and Ti–O–C bonding is formed [31]. For the C 1s of TG40s, the C–C and C–O shift to lower binding energies of 284.5 and 285.7 eV, as shown in Fig. 8b. This phenomenon represents that the carbon network of C–C and C–O are weakened and hence bonds well with TiO_2 dopants and lastly Ti–O–C bond is formed [32]. Additionally, the disappearance of C=O in TG40s sample is due to that the region is fully covered by O=C–O and O=C–O–Ti bonding is formed.

Likewise, the O 1s spectra of rGO nanosheet and TG40s sample are shown in Fig. 8c, d, respectively. In the O 1s spectrum of rGO nanosheet, the peak at 531.6 eV is assigned to C=O bond whereas the peak at 533.3 eV is ascribed to C–O bond. The C=O and C–O bonds after

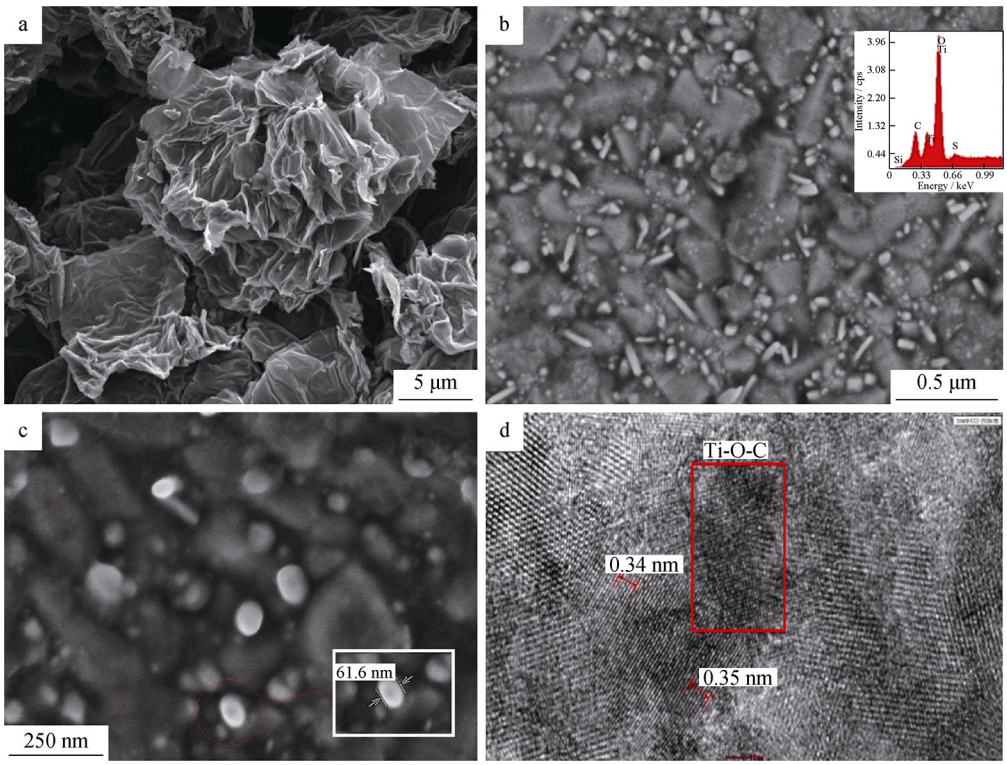

Fig. 6 FESEM images of **a** rGO nanosheet, **b** TiO_2–rGO nanocomposite sputtered with 40 s (TR40s) with inset EDX results, **c** measurement of TiO_2 nanoparticles within sample-TG40s and **d** HRTEM images for TG40s sample

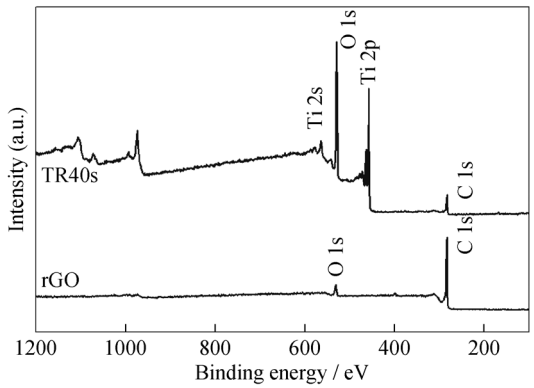

Fig. 7 XPS wide scan spectra of rGO nanosheet and TiO_2–rGO nanocomposite sputtered with 40 s (TR40s)

sputtering for 40 s disappear while TiO_2, OH and H_2O at 530.5, 531.1 and 532.4 eV, respectively, present. The phenomena are attributed to the attendance of Ti–O–C bond in TG40s [33, 34]. This result implements that TiO_2 is fully implanted into rGO nanosheet, thus proving the interaction among C, O and Ti after ion implantation process. For the Ti 2p spectrum of TG40s sample, it could be divided into several contributions corresponding to the different oxidation states of Ti. In Fig. 8e, the Ti $2p_{3/2}$ and Ti $2p_{1/2}$ peaks have binding energies of 458.3 and 464.1 eV, respectively. Moreover, Ti^{3+} peak at binding energy of 459.4 eV appears. Besides, the chemical state shift of Ti $2p_{3/2}$ to Ti $2p_{1/2}$ peak is 5.8 eV. The position of Ti 2p peak of TG40s is attributed to that no Ti–C bonding is formed between rGO and TiO_2–rGO nanocomposites [32].

A *J*–*V* characteristic of DSSCs device based on rGO nanosheet and TiO_2–rGO nanocomposite sputtered for different time is shown in Fig. 9 and the performance is summarised in Table 2. As seen, power conversion efficiency (η) values increase from 6.05% to 8.78% with an increase in sputtering time. A maximum η of 8.78% is obtained for TG40s. It is indicated that incorporating TiO_2 dopants into rGO nanosheet could further enhance the photocatalytic and charge transfer properties. However, the sample subjected for 60-s sputtering exhibits poor PCE of 5.39%. This is attributed to the overcharge recombination losses generated by excessive TiO_2 dopants on the rGO nanosheet and resulted in high charge transportation resistance within the TiO_2–rGO nanocomposite [35]. Finally, the η values decide the working DSSCs device performance. Formation of TiO_2–rGO nanocomposite as the photoanodes using this RF magnetron sputtering technique could deal with a higher PCE in DSSCs as compared to others deposition/incorporation technique. Furthermore, Ti^{4+} could accelerate with high energy (1 MeV) and implant into the rGO nanosheet in a short time while some

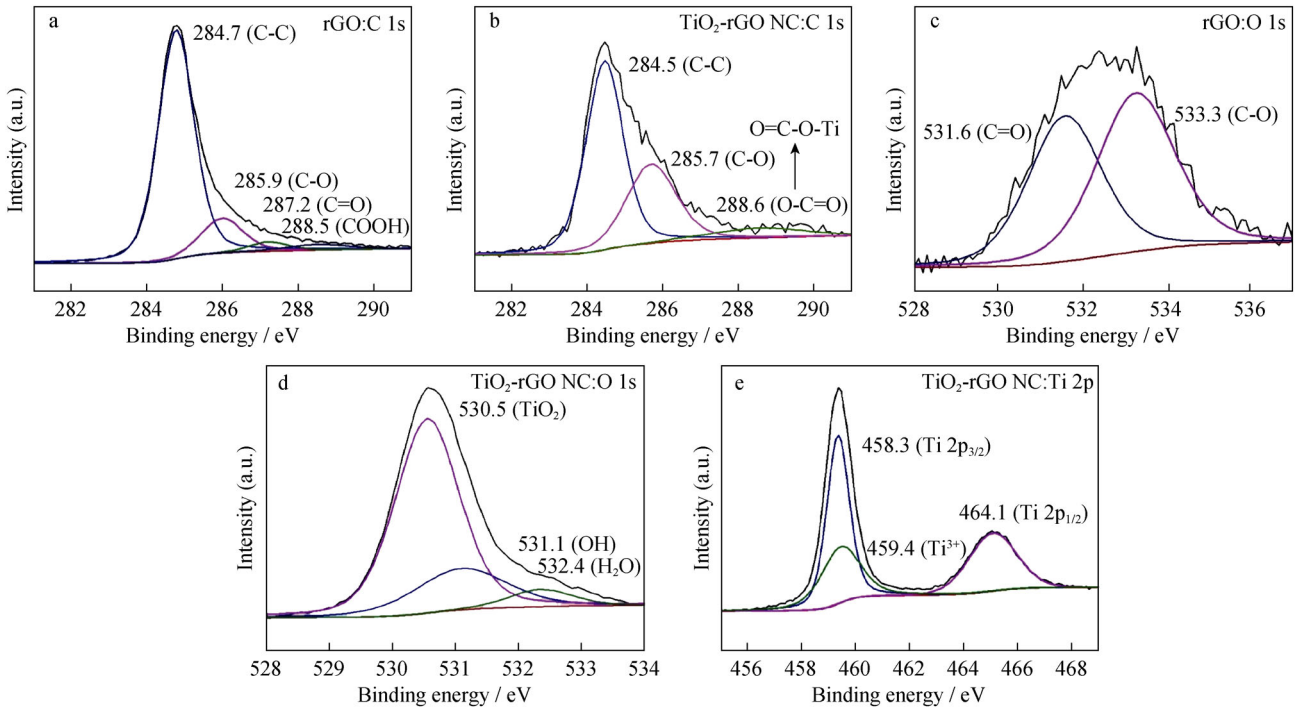

Fig. 8 High-resolution XPS spectra of C 1s for **a** rGO and **b** TiO_2–rGO nanocomposite sputtered with 40 s (TR40s); high-resolution XPS spectra of O 1s for **c** rGO and **d** TiO_2–rGO nanocomposite sputtered with 40 s (TR40s); **e** high-resolution XPS spectra of Ti 2p for TG40s

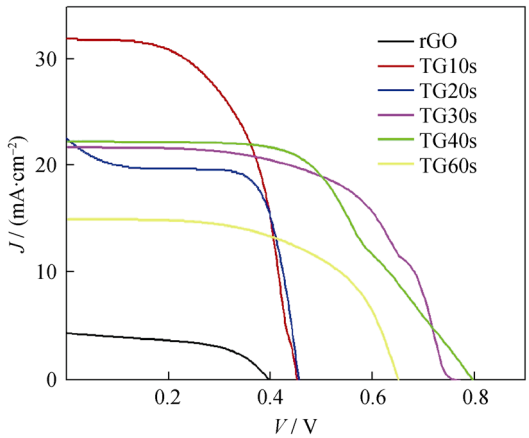

Fig. 9 *J*–*V* curves of DSSCs-based rGO and rGO with implantation time from 10 to 60 s

of Ti^{4+} could penetrate deeply into the lattice of rGO to form TiO_2–rGO nanocomposite.

4 Conclusion

The present work demonstrates a strongly beneficial effect of RF magnetron sputtering to incorporate small TiO_2 dopants on rGO nanosheets for improving the photovoltaic performance of DSSCs device compared with that of the pure rGO nanosheets. Based on the results obtained, the formation of TiO_2–rGO nanocomposite after subjecting 40-s sputtering duration exhibits a maximum PCE of 8.78% in DSSCs device. The highest PCE of DSSCs device is mainly attributed to the high efficient of photo-induced

Table 2 Typical photovoltaic performance of DSSCs with rGO and effect of Ti ion implantation duration

Samples	J_{sc}/(mA·cm^{-2})	V_{oc}/V	J_{max}/(mA·cm^{-2})	V_{max}/V	*ff*/%	P_{max}/(mS·cm^{-2})	η/%
rGO	4.34	0.39	1.91	0.35	0.40	0.68	0.68
TG10s	32.00	0.45	0.40	15.20	0.42	6.05	6.05
TG20s	22.70	0.46	0.40	15.35	0.59	6.17	6.17
TG30s	21.81	0.76	0.40	20.62	0.50	8.29	8.29
TG40s	22.39	0.80	0.40	21.81	0.49	8.78	8.78
TG60s	15.08	0.65	0.40	13.48	0.55	5.39	5.39

J_{max} maximum current density, V_{mp} maximum voltage and P_{max} maximum power

charge carriers separation within the bulk of TiO_2–rGO nanocomposite. In addition, this condition is also ascribed to the lowest estimated bandgap with 2.60 eV for the sample TG40s, which indicates the formation of Ti–O–C bonds associated to the closer CB between rGO and FTO glass. Such mechanistic understanding and findings are very important for improving the DSSCs device performance, which may be used to realise the direct energy transfer from photons to chemical energy.

Acknowledgements This work was financially supported by the University Malaya Prototype Grant (No. RU005G-2016), the Transdisciplinary Research Grant Scheme, TRGS (No. TR002A-2014B), the University Malaya Research Grant (No. RP045B-17AET) and the Global Collaborative Programme-SATU Joint Research Scheme from the University of Malaya (No. ST007-2017).

References

[1] Chen B, Sha J, Li W, He F, Liu E, Shi C. Graphene oxide-assisted synthesis of microsized ultrathin single-crystalline anatase TiO_2 nanosheets and their application in dye-sensitized solar cells. ACS Appl Mater Interfaces. 2016;8(4):2495.

[2] Lim SP, Pandikumar A, Huang NM, Lim HN. Reduced graphene oxide–titania nanocomposite-modified photoanode for efficient dye-sensitized solar cells. Int J Energy Res. 2015;39(6):812.

[3] Tang YB, Lee CS, Xu J, Liu ZT, Chen ZH, He Z. Incorporation of graphenes in nanostructured TiO_2 films via molecular grafting for dye-sensitized solar cell application. ACS Nano. 2010;4(6):3482.

[4] Guo J, Li Y, Zhu S, Chen Z, Liu Q, Zhang D. Synthesis of WO_3@graphene composite for enhanced photocatalytic oxygen evolution from water. Rsc Adv. 2012;2(4):1356.

[5] Low FW, Lai CW. Recent developments of graphene–TiO_2 composite nanomaterials as efficient photoelectrodes in dye-sensitized solar cells: a review. Renew Sustain Energy Rev. 2018;82(1):103.

[6] Chang BYS, Huang NM, An'amt MN, Marlinda AR, Norazriena Y, Muhamad MR. Facile hydrothermal preparation of titanium dioxide decorated reduced graphene oxide nanocomposite. Int J Nanomed. 2012;7:3379.

[7] Liang D, Cui C, Hu H, Wang Y, Xu S, Ying B. One-step hydrothermal synthesis of anatase TiO_2/reduced graphene oxide nanocomposites with enhanced photocatalytic activity. J Alloys Compd. 2014;582:236.

[8] Shen J, Yan B, Shi M, Ma H, Li N, Ye M. One step hydrothermal synthesis of TiO_2-reduced graphene oxide sheets. J Mater Chem. 2011;21(10):3415.

[9] Zhang Y, Zhang N, Tang ZR, Xu YJ. Improving the photocatalytic performance of graphene–TiO_2 nanocomposites via a combined strategy of decreasing defects of graphene and increasing interfacial contact. Phys Chem Chem Phys. 2012;14(25):9167.

[10] Liu Y. Hydrothermal synthesis of TiO_2–RGO composites and their improved photocatalytic activity in visible light. RSC Adv. 2014;4(68):36040.

[11] Ha NT, Long PD, Trung NT, Hong LV. Graphene effect on efficiency of TiO_2-based dye sensitized solar cells (DSSC). Commun Phys. 2016;26(1):43.

[12] Xiang Q, Yu J, Jaroniec M. Graphene-based semiconductor photocatalysts. Chem Soc Rev. 2012;41(2):782.

[13] Chong SW, Lai CW, Hamid SBA. Green preparation of reduced graphene oxide using a natural reducing agent. Ceram Int. 2015;41(8):9505.

[14] Sun S, Gao L, Liu Y. Enhanced dye-sensitized solar cell using graphene–TiO_2 photoanode prepared by heterogeneous coagulation. Appl Phys Lett. 2010;96(8):083113.

[15] Zhu M, Li X, Liu W, Cui Y. An investigation on the photoelectrochemical properties of dye-sensitized solar cells based on graphene–TiO_2 composite photoanodes. J Power Sources. 2014;262:349.

[16] Zhang Y, Wang C, Yuan Z, Zhang L, Yin L. Reduced graphene oxide wrapped mesoporous hierarchical TiO_2–CdS as a photoanode for high-performance dye-sensitized solar cells. Eur J Inorg Chem. 2017;2017(16):2281.

[17] He Z, Guai G, Liu J, Guo C, Loo JSC, Li CM, Tan TTY. Nanostructure control of graphene-composited TiO_2 by a one--step solvothermal approach for high performance dye-sensitized solar cells. Nanoscale. 2011;3(11):4613.

[18] Fan J, Liu S, Yu J. Enhanced photovoltaic performance of dye-sensitized solar cells based on TiO_2 nanosheets/graphene composite films. J Mater Chem. 2012;22(33):17027.

[19] Zhao J, Wu J, Yu F, Zhang X, Lan Z, Lin J. Improving the photovoltaic performance of cadmium sulfide quantum dots-sensitized solar cell by graphene/titania photoanode. Electrochim Acta. 2013;96:110.

[20] Low FW, Lai CW, Hamid SBA. Surface modification of reduced graphene oxide film by Ti ion implantation technique for high dye-sensitized solar cells performance. Ceram Int. 2017;43(1):625.

[21] Shu W, Liu Y, Peng Z, Chen K, Zhang C, Chen W. Synthesis and photovoltaic performance of reduced graphene oxide–TiO_2 nanoparticles composites by solvothermal method. J Alloys Compd. 2013;563:229.

[22] Kim H-N, Yoo H, Moon JH. Graphene-embedded 3D TiO_2 inverse opal electrodes for highly efficient dye-sensitized solar cells: morphological characteristics and photocurrent enhancement. Nanoscale. 2013;5(10):4200.

[23] Tang B, Hu G. Two kinds of graphene-based composites for photoanode applying in dye-sensitized solar cell. J Power Sources. 2012;220:95.

[24] Low FW, Lai CW, Hamid SBA. Easy preparation of ultrathin reduced graphene oxide sheets at a high stirring speed. Ceram Int. 2015;41(4):5798.

[25] Low FW, Lai CW, Hamid SBA. Study of reduced graphene oxide film incorporated of TiO_2 species for efficient visible light driven dye-sensitized solar cell. J Mater Sci Mater Electron. 2017;28(4):3819.

[26] Nouri E, Mohammadi MR, Lianos P. Impact of preparation method of TiO_2–RGO nanocomposite photoanodes on the performance of dye-sensitized solar cells. Electrochim Acta. 2016;219:38.

[27] Babu SG, Vinoth R, Kumar DP, Shankar MV, Chou H-L, Vinodgopal K. Influence of electron storing, transferring and shuttling assets of reduced graphene oxide at the interfacial copper doped TiO_2 p–n heterojunction for increased hydrogen production. Nanoscale. 2015;7(17):7849.

[28] Song J, Yin Z, Yang Z, Amaladass P, Wu S, Ye J. Enhancement of photogenerated electron transport in dye-sensitized solar cells with introduction of a reduced graphene oxide–TiO_2 junction. Chem A Eur J. 2011;17(39):10832.

[29] Tang B, Hu G, Gao H, Shi Z. Three-dimensional graphene network assisted high performance dye sensitized solar cells. J Power Sources. 2013;234:60.

[30] Cheng G, Akhtar MS, Yang O-B, Stadler FJ. Novel preparation of anatase TiO_2@ reduced graphene oxide hybrids for

high-performance dye-sensitized solar cells. ACS Appl Mater Interfaces. 2013;5(14):6635.
[31] Xiang Q, Yu J, Jaroniec M. Enhanced photocatalytic H_2-production activity of graphene-modified titania nanosheets. Nanoscale. 2011;3(9):3670.
[32] Haldorai Y, Rengaraj A, Kwak CH, Huh YS, Han Y-K. Fabrication of nano TiO_2@ graphene composite: reusable photocatalyst for hydrogen production, degradation of organic and inorganic pollutants. Synth Met. 2014;198:10.
[33] Tsai TH, Chiou SC, Chen SM. Enhancement of dye-sensitized solar cells by using graphene–TiO_2 composites as photoelectrochemical working electrode. Int J Electrochem Sci. 2011;6(8):3333.
[34] Shanmugam M, Durcan C, Gedrim RJ, Bansal T, Yu B. Oxygenated-graphene-enabled recombination barrier layer for high performance dye-sensitized solar cell. Carbon. 2013;60:523.
[35] Lai CW, Low FW, Chong SW, Wong PPC, Siddick BM, Siti Z. An overview: recent development of titanium dioxide loaded graphene nanocomposite film for solar application. Curr Org Chem. 2015;19(19):1882.